# Structural and optical properties evolution in pressure-induced amorphization of metal-organic framework ZIF-8

Xin Huang (黄 鑫)[1,2], Jin He (何 进)[1,3], Yiguang Jiang (姜益光)[1], Zhuocheng Chen (陈卓成)[4], Xing Duan (段 星)[1,5*], and Long Zhang (张 龙)[1,3,6**]

[1] CAS Key Laboratory of Materials for High Power Laser, Shanghai Institute of Optics and Fine Mechanics, Chinese Academy of Sciences, Shanghai 201800, China

[2] College of Materials Science and Optoelectronics Engineering, University of Chinese Academy of Sciences (UCAS), Beijing 100049, China

[3] Hangzhou Institute for Advanced Study, UCAS, Hangzhou 310024, China

[4] School of Materials and Chemistry, University of Shanghai for Science and Technology, Shanghai 200093, China

[5] Center of Advanced Optoelectronic Materials and Devices, Key Laboratory of Novel Materials for Sensor of Zhejiang Province, College of Materials and Environmental Engineering, Hangzhou Dianzi University, Hangzhou 310018, China

[6] Collaborative Innovation Center of IFSA (CICIFSA), Shanghai Jiao Tong University, Shanghai 200240, China

*Corresponding author: star1987@hdu.edu.cn
**Corresponding author: lzhang@siom.ac.cn
Received April 16, 2022 | Accepted May 17, 2022 | Posted Online June 14, 2022

Zeolitic imidazolate framework-8 (ZIF-8), a metal-organic framework (MOF) with a non-centrosymmetric crystal structure, exhibits nonlinear optics (NLO) properties and can act as the nanoporous matrix of guest molecules. Amorphization of ZIF-8 can be achieved by pressure or high temperature. Both crystalline and amorphous states have their inherent features for optical applications. The effects of the crystalline-amorphous transition on the structural and optical properties under pressure were investigated in detail. Amorphization leads to the destruction of the ZIF-8 lattice structure, collapse of pores, and the change of spatial symmetry, which in turn alters the NLO properties of ZIF-8 and the luminescence properties of the guest Eu cations. Our results establish the structure–optical properties relationship in the amorphization process and provide new clues in designing novel MOFs optical materials.

Keywords: ZIF-8; structure; optical properties; pressure.
DOI: 10.3788/COL202220.091603

## 1. Introduction

Metal-organic frameworks (MOFs) have well-defined units containing both inorganic and organic constituent elements, rich topologies, easily tunable porous structures, and extremely high specific surface area[1,2]. Because of their diverse structures and highly tunable pores, MOFs are able to cover the entire pore size interval between microporous zeolites and mesoporous silica, allowing them to have a wide range of applications in gas storage, catalysis, drug delivery, and photoluminescence (PL)[3–7]. MOFs have evolved into a class of promising optical functional materials in recent years. The pores of MOFs can be used to encapsulate a large number of guest molecules (such as nanoparticles, metal complexes, and organic dyes) to construct luminescent MOFs materials[8,9]. MOFs also exhibit nonlinear optics (NLO) properties such as multi-order harmonics, multi-photon

pumping, and data storage. Owing to the multi-optical unit properties, MOFs not only inherit the high NLO properties of organic ligands, but also generate metal-to-ligand charge-transfer transitions. Furthermore, the highly ordered frameworks and designable pores can confer spatial regulation and confinement of guest dipolar molecules, enabling the directional alignment and inducing harmonic generation responses[10,11].

Most MOFs materials are in a crystalline state. Over 60,000 crystalline MOFs materials have been identified from synthesis. In recent years, amorphous MOFs (aMOFs) have also gradually become a hot topic[12,13]. The facile tunable MOFs structure facilitates precise tuning of the pore size distribution and pore structure of the amorphous state[14]. Isotropy and enhanced strength of aMOF are important for optical applications as well[15]. Either the crystalline or amorphous state has its

inherent feature for optical applications. Therefore, studying the crystalline-amorphous transition and its influence on optical properties in MOFs is of significance for designing optical functional MOFs.

Zeolitic imidazolate framework-8 (ZIF-8) combines the advantages of a traditional zeolite structure and novel MOFs materials with high crystallinity, strong thermal stability, large specific surface area and pore volume, and high porosity[16,17]. ZIF-8 can be used as a host to load luminescent guest species to construct novel optical materials. In addition, ZIF-8 has superior NLO properties owing to its non-centrosymmetric crystal structure. The amorphization of ZIF-8 can be achieved by pressure, providing us with a good platform to study the structural and optical properties evolution in crystalline-amorphous transition[18–23].

In this Letter, we investigated the evolution in structural and optical properties of ZIF-8 crystals during pressure-induced amorphization. We carried out a battery of characterizations including powder X-ray diffraction (PXRD), scanning electron microscopy (SEM), $N_2$ adsorption measurement, second-harmonic signal measurement, and PL spectroscopy. The structural evolution of ZIF-8 crystals under pressure has been revealed. The optical properties of ZIF-8 during the crystal-amorphous transition, including second-harmonic generation (SHG) NLO properties, guest-host luminescence, for example, encapsulated with Eu cations, have been investigated in detail. The structure–optical properties relationship has been established to shed new light on the design of optical functional MOFs materials.

## 2. Experimental Method

### 2.1. Crystalline ZIF-8

A solid mixture of $Zn(NO_3)_2 \cdot 6H_2O(0.365\,g)$ and 2-methylimidazole (H-MeIM) (0.250 g) was dissolved in 40 mL of dimethylformamide (DMF). Solution was poured into a 100 mL blue cap bottle and stirred for 30 min. The bottle was sealed, and solvothermal synthesis was carried out at 130°C for 48 h. After a complete reaction, the solution was allowed to cool to ambient temperature overnight. The resultant ZIF-8 crystals were filtered off the precursor solution and washed three times with 50 mL of DMF, followed by drying in an oven at 130°C for 12 h.

### 2.2. Crystalline Eu at ZIF-8

$Eu(NO_3)_3 \cdot 6H_2O$ was dissolved in 10 mL of DMF, and the ZIF-8 crystals were poured into the solution and kept for 72 h. The crystals were filtered out of the solution, washed three times with 10 mL of DMF, and dried at 130°C for 12 h.

### 2.3. Amorphization of ZIF-8

Amorphization of the ZIF-8 crystals was done by the dry press molding method or cold isostatic pressing. When the applied pressure is lower than 50 MPa, we only used the hydraulic powder machine. The pressure was held at 20 MPa and 50 MPa for

5 min, respectively. When the pressure is higher than 50 MPa, the hydraulic press can no longer meet the demand, and we need to use a cold isostatic press. The pressure was held at 100 MPa and 200 MPa for 5 min, respectively.

X-ray diffraction (XRD) patterns were recorded using a Bruker D8 ADVANCE diffractometer with Cu Ka radiation (40 kV, 30 mA, 2 deg/min from 5 to 50 deg, $\lambda = 0.015405$ nm). The microstructure of the sample was observed using field emission SEM. A specific surface area was obtained using a Micromeritics ASAP 2020 instrument to measure the $N_2$ adsorption isotherm at 77 K based on the Brunauer–Emmett–Teller (BET) method. Prior to the $N_2$ adsorption and the mercury porosimetry analysis, all samples were evacuated overnight for 24 h at 120°C under vacuum. SHG measurement was performed with an MStarter 100 Ultrafast confocal microscope, in which the excitation wavelength was 1030 nm (Metatest Co., Ltd., China). The PL spectra were recorded on an Edinburgh FLS920 fluorescence spectrophotometer equipped with a Xe-900 lamp as the excitation source. The decay curves were collected using an FLS920 instrument with an nF900 flash lamp as the excitation source.

## 3. Result and Discussion

### 3.1. Amorphization of ZIF-8 crystals

We promote amorphization of ZIF-8 crystals by continuously increasing pressure. The PXRD patterns of ZIF-8 crystals under different pressure clearly show the transition of ZIF-8 from the crystalline to amorphous state, as shown in Fig. 1. The characteristic diffraction peaks of the unpressurized ZIF-8 crystals were in good agreement with the XRD peaks of the simulated pattern formed from the crystals structure. The diffraction peaks are sharp, indicating that the prepared samples are ZIF-8 crystals with high purity and good crystallinity[23]. When pressurized at 20 MPa, the crystal structure of ZIF-8 was destroyed, and the position of the Bragg peak remained unchanged, but the
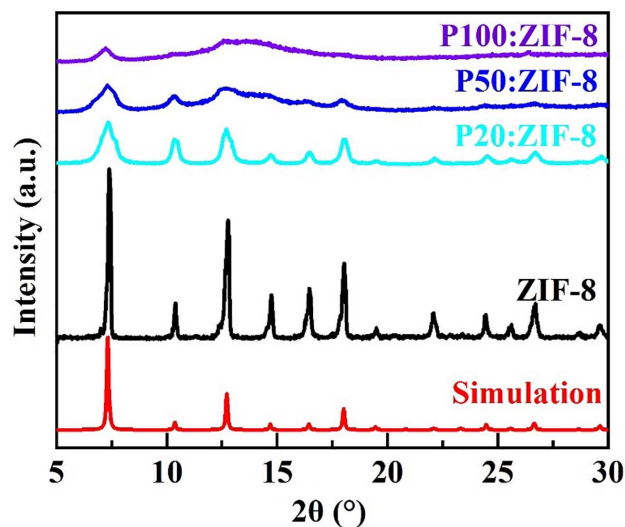


**Fig. 1.** PXRD patterns of ZIF-8 under different pressure.

peak intensity decreased, and the peak width increased. When the pressure increased to 50 MPa, some characteristic peaks disappeared, and the peak shape became smoother. At further pressure up to 100 MPa, there were no sharp Bragg peaks in the XRD pattern, but a broad peak envelope appeared, indicating that the long-range order of the ZIF-8 crystals was destroyed, and amorphization was achieved.

Under the pressure, the ZIF-8 crystals will gradually fragment into smaller powder particles. In order to observe the morphological changes of ZIF-8 crystals during amorphization, the crystals were characterized by SEM, as shown in Fig. 2. Figure 2(a) shows the morphology and distribution of the main elements of ZIF-8 crystals without stress. Grain growth is relatively regular, the grain size is about 10 μm, the aggregation of C, N, and Zn elements is relatively obvious, and the aggregation corresponds to the location of the ZIF-8. After being subjected to 50 MPa pressure, the structure of the ZIF-8 crystal was destroyed, and the whole ZIF-8 crystal was crushed into particles of different sizes, as shown in Fig. 2(b). Because the ZIF-8 crystal particles still retain part of their structure, the Bragg peaks in Fig. 1 are smoothed, but do not completely disappear.

We analyzed the porosity and Brunauer–Emmett–Teller (BET) surface areas of the prepared samples by using $N_2$ adsorption at 77 K, as shown in Fig. 3. The adsorption curve and desorption curve of the samples almost overlapped without significant hysteresis, and the shape belonged to the typical I adsorption-desorption isotherm[24]. This was a typical adsorption curve of microporous substances, indicating that the samples were indeed microporous (porosity diameter $<2$ nm)[25]. $N_2$ adsorption rose sharply with increasing pressure at low $P/P_0$ because of the strong interaction between the adsorbent and the pore wall in microporous structured materials. When the pressure increased to a certain level at $P/P_0$ of about 0.1, the adsorption gradually smoothed. A large increase in $N_2$ adsorption is shown at higher pressure close to the saturation pressure due to the condensation of $N_2$ molecules on the outer
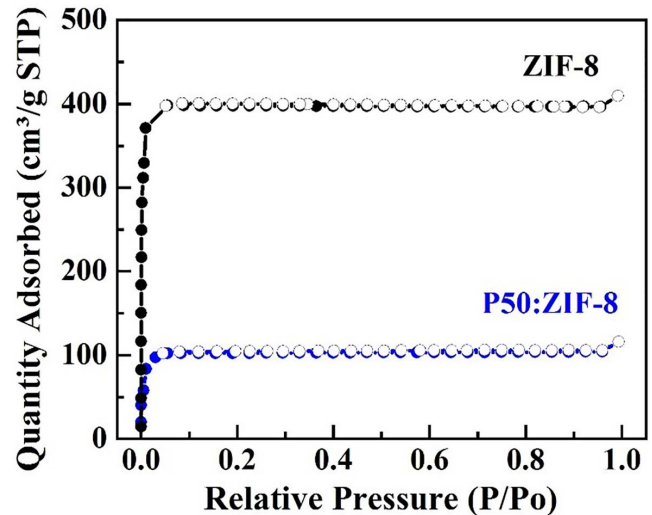
**Fig. 3.** $N_2$ adsorption isotherms for ZIF-8 before (black) and after (blue) pressurization. Solid circles indicate adsorption, while hollow circles indicate desorption.

surface of the material[25]. Measurements of $N_2$ adsorption showed that the BET surface area decreased significantly after pressurization, from 1008 $m^2/g$ to 346 $m^2/g$, and the total pore volume also decreased from 0.342 $cm^3/g$ to 0.136 $cm^3/g$. This fact suggests a gradual amorphization when using higher pressure, causing the collapse of porosity. In addition, the BET surface area can be maintained at about 350 $m^2/g$ after pressurization, because with the evolution of the ZIF-8 pore shape to amorphization, there are still some pores essentially intact, while the channels connecting them become narrow[25,26]. This can also be seen from the measurement results of PXRD and SEM.

ZIF-8 consists of 2-methylimidazolate coordinated to a tetrahedral-linked metal center $Zn^{2+}$, which results in a zeolite-like topology. ZIF-8 demonstrates a strong intrinsic SHG signal due to its non-centrosymmetric cubic I-43m space group symmetry[27]. It has a higher value of the second NLO coefficient than commercial inorganic crystals of potassium dihydrogen phosphate (KDP)[28]. The non-centrosymmetric crystal structure of ZIF-8 is altered during the crystal-amorphous transition, leading to changes in its NLO properties. The average size of our prepared ZIF-8 crystals was optically estimated to be 10 μm, enabling us to detect the SHG signal[27,28]. Figure 4 represents the SHG spectra of the samples subjected to different pressures. The excitation wavelength was 1030 nm, and the emission wavelength was at 515 nm. The intensity of the SHG signal gradually weakened with the increase of pressure. After pressure-induced amorphization, the structure of ZIF-8 crystals was disrupted, and the symmetry of its space group was also destroyed, resulting in the weakening of the SHG signal.

### 3.2. Amorphization of Eu at ZIF-8 crystals

Based on the guest-host luminescence approach, we prepared Eu at ZIF-8 to further investigate the evolution of the structural and
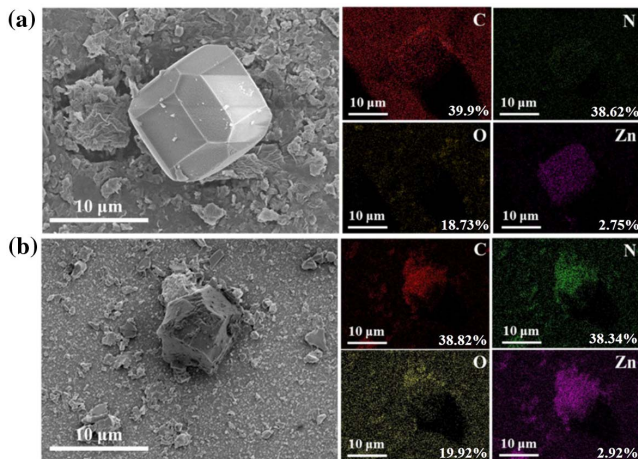
**Fig. 2.** SEM images and elemental distribution of ZIF-8 (a) before and (b) after pressurization. The atomic percentage of each element is shown at the bottom right of the images.
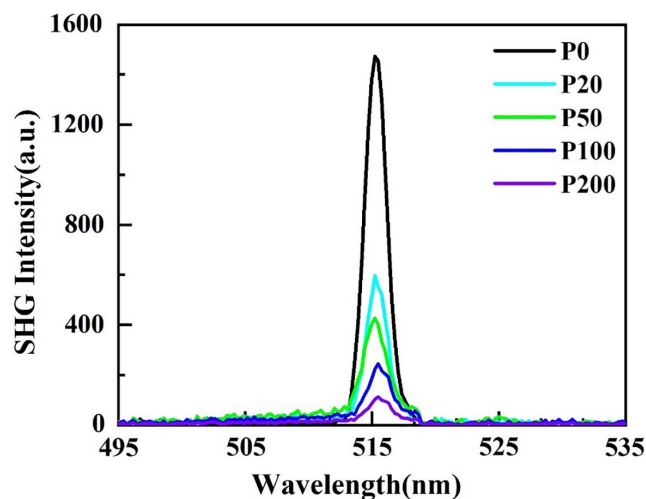
**Fig. 4.** SHG signal of ZIF-8 under different pressure excited by IR laser radiation (1030 nm central wavelength, 150 fs pulse duration, 50 mW, 80 MHz repetition rate).
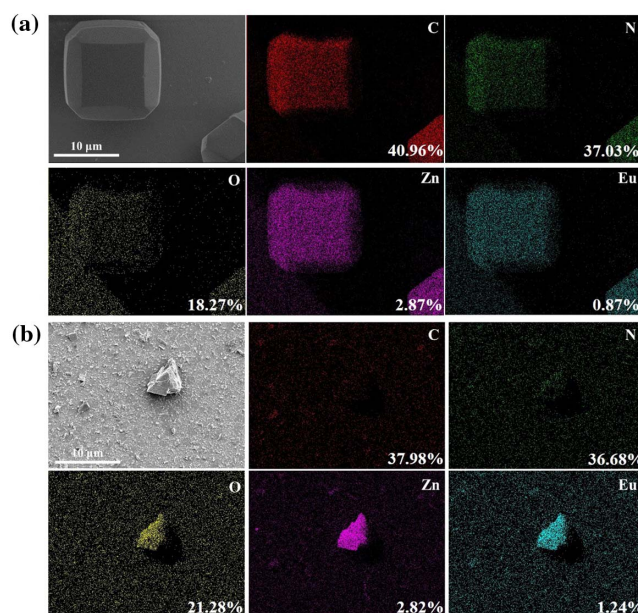


**Fig. 5.** SEM images and elemental distribution of Eu at ZIF-8 (a) before and (b) after pressurization. The atomic percentage of each element is shown at the bottom right of the images.

optical properties of ZIF-8 crystals during the pressure-induced amorphization. The $Eu^{3+}$ ions were filled into the pores of ZIF-8 by prolonged soaking. Eu ions have turned out to be a promising medium for efficient infrared emission with a perspective of application in the respective laser and optical amplifier devices[29–31]. In addition, $Eu^{3+}$ is otherwise known as the most sensitive probe to the structure/symmetry of rare-earth doping sites[31]. By studying the split of the respective narrow emission bands in the crystalline field, different sites of dopants and their symmetry can be identified[31,32]. In this work, in addition to the photofunctionalization of ZIF-8 by loading $Eu^{3+}$ to study the optical properties, we also used $Eu^{3+}$ as a probe to reveal the changes in the structure and symmetry of ZIF-8 during amorphization.

To confirm whether $Eu^{3+}$ ions had entered the pores of ZIF-8 crystals, an elemental scan of the sample was performed. From Fig. 5(a), we can see that $Eu^{3+}$ ions were successfully immersed into ZIF-8. The crystal morphology is relatively regular in shape and still around 10 μm in size. After being subjected to a pressure of 50 MPa, Eu at ZIF-8 was also crushed into small irregular particles. As the structure was damaged, some of the $Eu^{3+}$ ions were released. Figure 6(a) shows that there is no obvious change in the XRD peaks of ZIF-8 crystals after loading with $Eu^{3+}$ ions. $Eu^{3+}$ ions are mainly loaded into the pores of ZIF-8 and do not destroy the lattice structure. Moreover, because of the support of $Eu^{3+}$ in the pores, the degree of amorphization of Eu at ZIF-8 is lower than that of ZIF-8 under the same pressure.

Compared with the ZIF-8 crystals, the BET surface area of Eu at ZIF-8 is reduced to 825 $m^2/g$. This is caused by the entry of $Eu^{3+}$ ions into the pores to occupy a definite pore volume. The BET area of Eu at ZIF-8 was reduced to 340 $m^2/g$, and the pore volume also decreased from 0.338 $cm^3/g$ to 0.148 $cm^3/g$ after pressure amorphization, as shown in Fig. 6(b). The changing trend of the $N_2$ adsorption of Eu at ZIF-8 after amorphization is consistent with that of the ZIF-8 sample.

In the matrix, the crystal field or chemical change around the rare-earth ions is closely related to the microenvironment around the rare-earth ions. A slight change can cause the luminescence intensity or spectral splitting of the rare-earth ions. The local environment of the luminescence center affects the structure and distribution of the observed lines[29,31]. The PL spectra of the Eu at ZIF-8 samples before and after pressure-induced amorphization are shown in Fig. 7. The PL spectrum consists of the electron rearrangement standard within the 4f shell layer (f–f transitions) of Eu, corresponding to the transitions from the $^5D_0$ to $^7F_J$ ($J = 0$–4) energy level[29,31,32]. The observed peaks at 578 nm, 591 nm, 616 nm, 651 nm, and 698 nm correspond to $^5D_0 \rightarrow {}^7F_0$, $^5D_0 \rightarrow {}^7F_1$, $^5D_0 \rightarrow {}^7F_2$, $^5D_0 \rightarrow {}^7F_3$, and $^5D_0 \rightarrow {}^7F_4$ transitions, respectively[32]. The emission spectra of the amorphous Eu at ZIF-8 samples have no change in the position of the center wavelength of the peaks, but the intensity of the emission spectra was significantly weaker. The ultrasensitive transition of $Eu^{3+}$ ions from $^5D_0 \rightarrow {}^7F_2$ is an electric dipole transition and is very sensitive to the changes in the surrounding
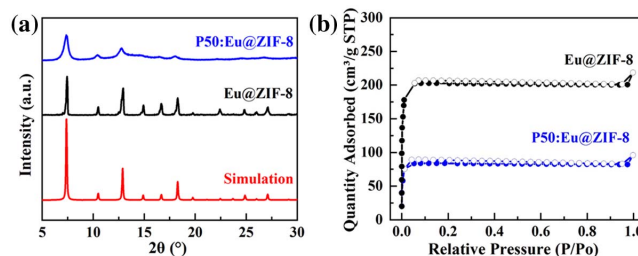


**Fig. 6.** (a) PXRD patterns and (b) $N_2$ adsorption isotherms of Eu at ZIF-8 before and after pressurization.
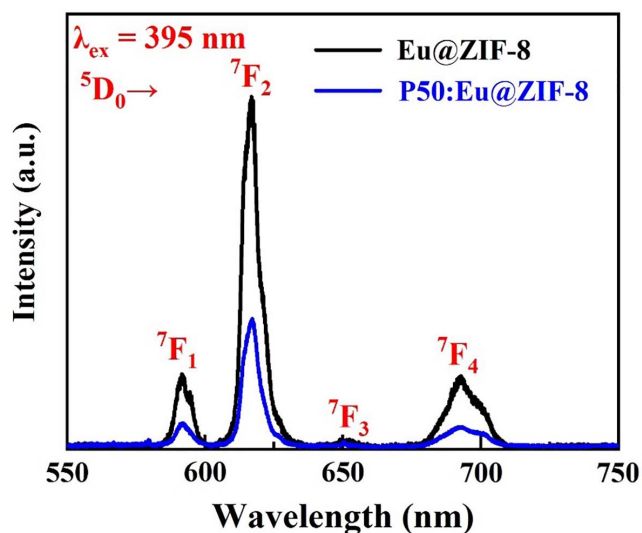
**Fig. 7.** PL spectra for Eu at ZIF-8 before (black) and after (blue) pressurization.

environment. However, the magnetic dipole transition of $^5D_0 \rightarrow$ $^7F_1$ is relatively less variable than the former and has no obvious dependence on the surrounding environment. Therefore, the ratio of transition intensity of $^5D_0 \rightarrow {}^7F_2$ to that of $^5D_0 \rightarrow {}^7F_1$ can be used to define a parameter to characterize the change of the coordination symmetry around $Eu^{3+}$. Define $R = I(^5D_0 \rightarrow {}^7F_2)/I(^5D_0 \rightarrow {}^7F_1)$ to analyze the crystallographic environment of the emission center and information on polyhedral distortion[31,32]. Although the emission peak intensity of the Eu at ZIF-8 decreased after pressurization, the $R$ value (6.364) was significantly greater than that before pressurization (5.995). This result suggests that the lattice symmetry around $Eu^{3+}$ ions decreases during amorphization. The environment around the $Eu^{3+}$ ions is changed, and the lattice structure of ZIF-8 is destroyed, leading to weakening of the luminescence.

## 4. Conclusions

We have induced amorphization of ZIF-8 by pressure to investigate the evolution of the structure and optical properties of ZIF-8 crystals during pressure-induced amorphization. At 20 MPa, the crystalline ZIF-8 already showed a tendency to amorphize. During the amorphization process, with increasing pressure, the lattice structure of ZIF-8 was gradually destroyed, the pores collapsed, and the BET surface area decreased significantly. The non-centrosymmetric crystal structure of ZIF-8 is altered during the crystal-amorphous transition, resulting in the decrease of SHG signal intensity. The amorphization effect on the guest-host luminescence behavior of ZIF-8 has been explored as well, via encapsulation with $Eu^{3+}$ cations, the luminescence of which would reflect the spatial symmetry evolution. Accompanied with the destruction of the crystal lattice and the spatial symmetry of Eu at ZIF-8, the evolution of Eu cations luminescence, including the decrease of PL intensity and the increase of $R$ ratio, has been observed. This work showed that

the change of the lattice field environment not only affects the NLO properties of ZIF-8 itself, but also the luminescence of the guest species. The structural evolution in ZIF-8 amorphization and the structure–optical properties relationship provide a new avenue for the development of optical functional MOFs materials.

## References

1. Y. Q. Tian, C. X. Cai, X. M. Ren, C. Y. Duan, Y. Xu, S. Gao, and X. Z. You, "The silica-like extended polymorphism of cobalt(II) imidazolate three-dimensional frameworks: X-ray single-crystal structures and magnetic properties," Chemistry **9**, 5673 (2003).
2. P. I. Saragi, T. Spehr, A. Siebert, T. F. Lieker, and J. Salbeck, "Spiro compounds for organic optoelectronics," Chem. Rev. **107**, 1011 (2007).
3. H. Kim, S. Yang, S. R. Rao, S. Narayanan, E. A. Kapustin, H. Furukawa, A. S. Umans, O. M. Yaghi, and E. N. Wang, "Water harvesting from air with metal-organic frameworks powered by natural sunlight," Science **356**, 430 (2017).
4. C. Li, K. Wang, J. Z. Li, and Q. C. Zhang, "Recent progress in stimulus-responsive two-dimensional metal–organic frameworks," ACS Mater. Lett. **2**, 779 (2020).
5. J. A. Mason, J. Oktawiec, M. K. Taylor, M. R. Hudson, J. Rodriguez, J. E. Bachman, M. I. Gonzalez, A. Cervellino, A. Guagliardi, C. M. Brown, P. L. Llewellyn, N. Masciocchi, and J. R. Long, "Methane storage in flexible metal–organic frameworks with intrinsic thermal management," Nature **527**, 357 (2015).
6. M. S. Denny, J. C. Moreton, L. Benz, and S. M. Cohen, "Metal–organic frameworks for membrane-based separations," Nat. Rev. Mater. **1**, 16078 (2016).
7. J. E. Mondloch, M. J. Katz, W. C. Isley, III, P. Ghosh, P. Liao, W. Bury, G. W. Wagner, M. G. Hall, J. B. DeCoste, G. W. Peterson, R. Q. Snurr, C. J. Cramer, J. T. Hupp, and O. K. Farh, "Destruction of chemical warfare agents using metal–organic frameworks," Nat. Mater. **14**, 512 (2015).
8. H. J. Li, H. J. He, J. C. Yu, Y. J. Cui, Y. Yang, and G. D. Qian, "Dual-band simultaneous lasing in MOFs single crystals with Fabry–Perot microcavities," Sci China Chem. **62**, 987 (2019).
9. Y. H. Wei, H. Y. Dong, C. Wei, W. Zhang, Y. L. Yan, and Y. S. Zhao, "Wavelength-tunable microlasers based on the encapsulation of organic dye in metal-organic frameworks," Adv. Mater. **28**, 7424 (2016).
10. J. C. Yu, Y. J. Cui, C. D. Wu, Y. Yang, Z. Y. Wang, M. O. Keeffe, B. L. Chen, and G. D. Qian, "Second-order nonlinear optical activity induced by ordered dipolar chromophores confined in the pores of an anionic metal-organic framework," Angew. Chem. Int. Ed. **51**, 10542 (2012).
11. S. Chen, S. Y. Yang, Y. Huang, W. Y. Jiao, G. H. Fan, and Y. C. Gao, "Wavelength-dependent nonlinear absorption of gold nanocages," Chin. Opt. Lett. **18**, 011901 (2020).
12. M. M. Wang, M. K. Zhang, W. W. Song, L. Zhou, X. Y. Wang, and Y. F. Tang, "Heteroatom-doped amorphous cobalt–molybdenum oxides as a promising catalyst for robust hydrogen evolution," Inorg. Chem. **61**, 5033 (2022).
13. A. C. Ghosh, A. Legrand, R. Rajapaksha, G. A. Craig, C. Sassoye, G. Balázs, D. Farrusseng, S. Furukawa, J. Canivet, and F. M. Wisser, "Rhodium-based metal–organic polyhedra assemblies for selective $CO_2$ photoreduction," J. Am. Chem. Soc. **144**, 3626 (2022).
14. H. Z. Wang, X. K. Pei, M. J. Kalmutzki, J. J. Yang, and O. M. Yaghi, "Large cages of zeolitic imidazolate frameworks," Acc. Chem. Res. **55**, 707 (2022).

15. A. Qiao, T. D. Bennett, H. Z. Tao, A. Krajnc, G. Mali, C. M. Doherty, A. W. Thornton, J. C. Mauro, G. N. Greaves, and Y. Z. Yue, "A metal-organic framework with ultrahigh glass-forming ability," Sci. Adv. **4**, 6827 (2018).
16. K. S. Park, Z. Ni, A. P. Côté, J. Y. Choi, R. D. Huang, F. J. Uribe-Romo, H. K. Chae, M. O. Keeffe, and O. M. Yaghi, "Exceptional chemical and thermal stability of zeolitic imidazolate frameworks," Proc. Natl. Acad. Sci. U.S.A. **103**, 10186 (2006).
17. J. J. Ren, T. R. Li, X. P. Zhou, X. Dong, A. V. Shorokhov, M. B. Semenov, V. D. Krevchik, and Y. H. Wang, "Encapsulating all-inorganic perovskite quantum dots into mesoporous metal organic frameworks with significantly enhanced stability for optoelectronic applications," Chem. Eng. J. **358**, 30 (2019).
18. G. N. Greaves and S. Sen, "Inorganic glasses, glass-forming liquids and amorphizing solids," Adv. Phys. **56**, 1 (2007).
19. T. D. Bennett, A. L. Goodwin, M. T. Dove, D. A. Keen, M. G. Tucker, E. R. Barney, A. K. Soper, E. G. Bithell, J. C. Tan, and A. K. Cheetham, "Structure and properties of an amorphous metal-organic framework," Phys. Rev. Lett. **104**, 115503 (2010).
20. R. N. Widmer, G. I. Lampronti, S. Anzellini, R. Gaillac, S. Farsang, C. Zhou, A. M. Belenguer, C. W. Wilson, H. Palmer, A. K. Kleppe, M. T. Wharmby, X. Yu, S. M. Cohen, S. G. Telfer, S. A. T. Redfern, F.-X. Coudert, S. G. MacLeod, and T. D. Bennett, "Pressure promoted low-temperature melting of metal–organic frameworks," Nat. Mater. **18**, 370 (2019).
21. A. S. Poryvaev, D. M. Polyukhov, and M. V. Fedin, "Mitigation of pressure-induced amorphization in metal-organic framework ZIF-8 upon EPR control," ACS Appl. Mater. Interfaces **12**, 16655 (2020).
22. M. Guo, H. B. He, K. Yi, S. Y. Shao, G. H. Hu, and J. D. Shao, "Optical characteristics of ultrathin amorphous Ge films," Chin. Opt. Lett. **18**, 103101 (2020).
23. T. D. Bennett and A. K. Cheetham, "Amorphous metal−organic frameworks," Acc. Chem. Res. **47**, 1555 (2014).
24. D. F. Jimenez, R. Galvelis, A. Torrisi, A. D. Gellan, M. T. Wharmby, P. A. Wright, C. M. Draznieks, and T. Düren, "Flexibility and swing effect on the adsorption of energy-related gases on ZIF-8: combined experimental and simulation study," Dalton Trans. **41**, 10752 (2012).
25. T. Tian, J. V. Garcia, T. D. Bennett, and D. F. Jimenez, "Mechanically and chemically robust ZIF-8 monoliths with high volumetric adsorption capacity," J. Mater. Chem. A **3**, 2999 (2015).
26. T. D. Bennett, S. Cao, J. C. Tan, D. A. Keen, E. G. Bithell, P. J. Beldon, T. Friscic, and A. K. Cheetham, "Facile mechanosynthesis of amorphous zeolitic imidazolate frameworks," J. Am. Chem. Soc. **133**, 14546 (2011).
27. S. V. Cleuvenbergen, I. Stassen, E. Gobechiya, Y. X. Zhang, K. Markey, D. E. De Vos, C. Kirschhock, B. Champagne, T. Verbiest, and M. A. Van Der Veen, "ZIF-8 as nonlinear optical material: influence of structure and synthesis," Chem. Mater. **28**, 3203 (2016).
28. Y. A. Mezenov, N. K. Kulachenkov, A. N. Yankin, S. S. Rzhevskiy, P. V. Alekseevskiy, V. D. Gilemkhanova, S. V. Bachinin, V. Dyachuk, and V. A. Milichko, "Polymer matrix incorporated with ZIF-8 for application in nonlinear optics," Nanomaterials **10**, 1036 (2020).
29. K. Driesen, V. K. Tikhomirov, and C. Gorller-walrand, "Eu$^{3+}$ as probe for rare earth dopant site structure in nano-glass ceramics," J. Appl. Phys. **102**, 024312 (2007).
30. X. M. Li, S. S. Zhou, R. F. Wei, X. Y. Liu, B. Q. Cao, and H. Guo, "Blue–green color-tunable emissions in novel transparent Sr$_2$LuF$_7$:Eu/Tb glass-ceramics for WLEDs," Chin. Opt. Lett. **18**, 051601 (2020).
31. G. H. Jia, P. A. Tanner, C. K. Duan, and J. Dexpert-Ghys, "Eu$^{3+}$ spectroscopy: a structural probe for yttrium orthoborate phosphors," J. Phys. Chem. C **114**, 2769 (2010).
32. D. V. Deyneko, I. V. Nikiforov, D. A. Spassky, Y. Y. Dikhtyar, S. M. Aksenov, S. Y. Stefanovich, and B. I. Lazoryak, "Luminescence of Eu$^{3+}$ as a probe for the determination of the local site symmetry in β-Ca$_3$(PO$_4$)$_2$-related structures," Cryst. Eng. Comm. **21**, 5235 (2019).